Electronic Coupling Between Perovskite Nanocrystal and Fullerene Modulates Hot Carrier Capture

Yusheng Li, Junke Jiang, Dandan Wang, Dong Liu, Shota Yajima, Hua Li, Akihito Fuchimoto, Hongshi Li, Guozheng Shi, Shuzi Hayase, et al.

ADVANCED FUNCTIONAL MATERIALS
www.afm-journal.de

Electronic Coupling Between Perovskite Nanocrystal and Fullerene Modulates Hot Carrier Capture

Yusheng Li, Junke Jiang, Dandan Wang, Dong Liu, Shota Yajima, Hua Li, Akihito Fuchimoto, Hongshi Li, Guozheng Shi, Shuzi Hayase, Shuxia Tao, Jiangjian Shi, Qingbo Meng,* Chao Ding,* and Qing Shen**

The efficient harnessing of hot carriers holds transformative potential for next-generation optoelectronic devices. Halide perovskites, with their remarkably long carrier lifetimes exceeding 10 picoseconds, stand at the forefront of this research frontier. Yet, a fundamental paradox persists: why does efficient hot carrier capture remain elusive despite these extended lifetimes? Here, this conundrum is unraveled by constructing a donor–acceptor model system: perovskite nanocrystal and fullerene hybrids. It is demonstrated that the challenge lies not only in the carrier lifetime itself but in the nature of the coupling between donor and acceptor components. Remarkably, it is discovered that the formation of ground-state complexes, with effective coupling across a wide energy range, not only overcomes the initially forbidden hot carrier capture within these hybrids but also dramatically enhances it, achieving a ≈76% hot carrier capture efficiency. This finding shifts the paradigm of hot carrier capture from extending carrier lifetimes to engineering donor–acceptor coupling, illuminating a path toward practical hot carrier applications.

1. Introduction

In semiconductor optoelectronics applications, a significant portion of absorbed photon energy is lost as heat before charge carriers can be collected, fundamentally limiting device efficiencies.[1,2] Hot carrier (HC) optoelectronics offers a paradigm-shifting approach to overcoming these limitations.[3–5] By harnessing charge carriers before they cool to lattice temperatures, HC-based devices have the potential to revolutionize a wide spectrum of applications. In photovoltaics, for example, the effective utilization of HCs could potentially double the Shockley–Queisser limit, pushing single-junction solar cell efficiencies from 33% to an unprecedented 66%.[4,6] Similarly, in photocatalysis, HCs could drive chemical reactions with unparalleled efficiency and selectivity.[7,8]

Recent advancements in halide perovskites, driven by their unique electron and phonon structures and favorable electron–phonon interactions, have positioned these materials at the forefront of HC research.[9–12] Their remarkably long HC lifetimes—exceeding 10 picoseconds in bulk and even longer in nanocrystals (NCs)—preserve the energetic states of carriers while allowing for propagation distances on the order of hundreds of nanometers.[13,14] These exceptional temporal and spatial characteristics, enabling HCs to readily reach material boundaries (**Figure 1a**), underscore the feasibility of next-generation devices that effectively harness a broad range of photon energies across

Y. Li, D. Wang, D. Liu, S. Yajima, H. Li, A. Fuchimoto, G. Shi, S. Hayase, C. Ding[++], Q. Shen
Faculty of Informatics and Engineering
The University of Electro-Communications
1-5-1 Chofugaoka, Chofu, Tokyo 182–8585, Japan
E-mail: ding@jupiter.pc.uec.ac.jp; shen@pc.uec.ac.jp

The ORCID identification number(s) for the author(s) of this article can be found under https://doi.org/10.1002/adfm.202415735

[+]Present address: Univ Rennes, INSA Rennes, CNRS, Institut FOTON – UMR 6082, Rennes F-35000, France

[++]Present address: Institute of New Energy and Low-Carbon Technology, Sichuan University, Chengdu 610065, P. R. China

DOI: 10.1002/adfm.202415735

J. Jiang[+], S. Tao
Materials Simulation and Modelling
Department of Applied Physics
Eindhoven University of Technology
Eindhoven 5600 MB, The Netherlands
E-mail: S.X.Tao@Tue.nl

H. Li
Institute of New Energy Materials Chemistry
School of Materials Science and Engineering
Nankai University
TongYan street 38, Jinnan District, Tianjin 300350, P. R. China

J. Shi, Q. Meng
Key Laboratory for Renewable Energy
Beijing Key Laboratory for New Energy Materials and Devices
Chinese Academy of Sciences
Beijing 100190, P. R. China
E-mail: qbmeng@iphy.ac.cn

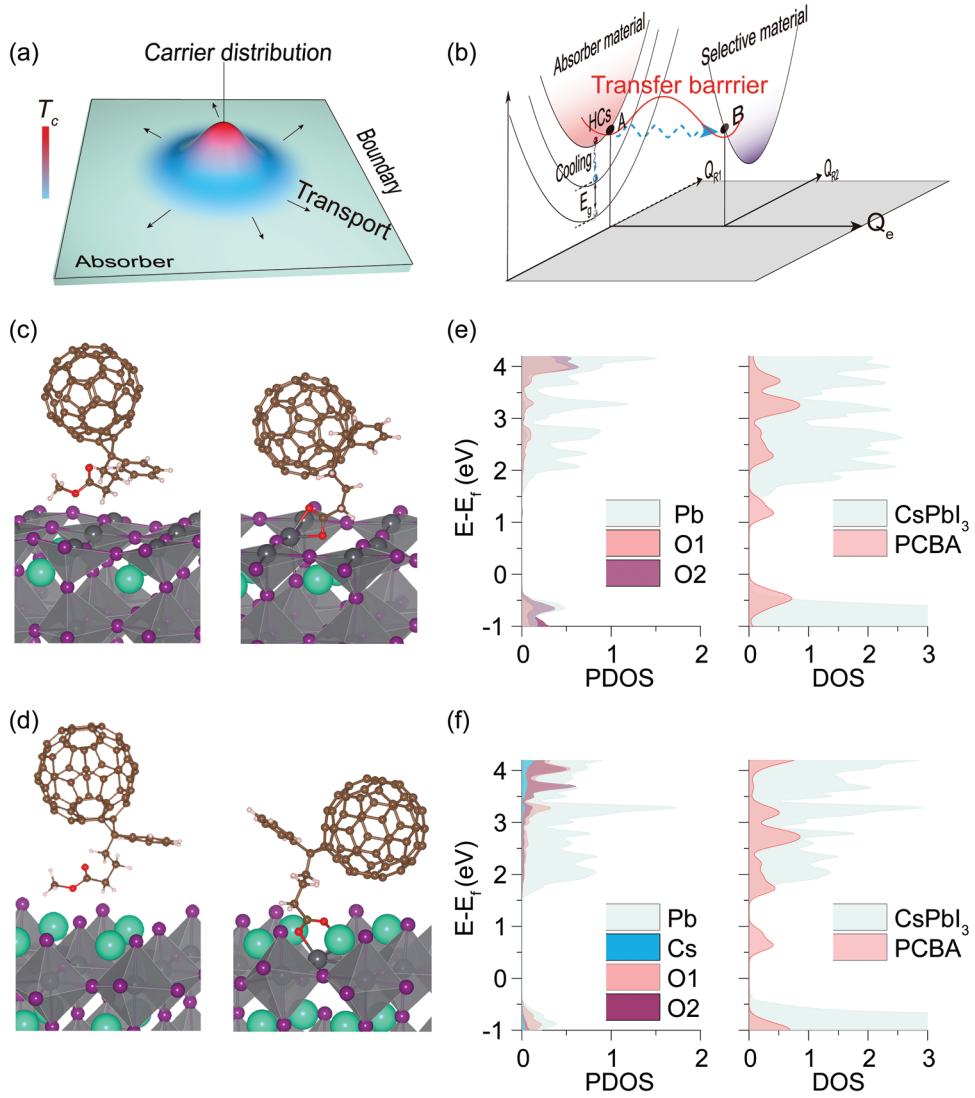

Figure 1. a) Schematic illustrating HC transportation in absorber materials, demonstrating how extended carrier lifetimes facilitate diffusion to boundaries. b) Diagram showing the impact of coupling on HC capture efficiency, Q_{R1} and Q_{R2} represent the configuration coordinates of the absorber and selective materials, respectively, Q_e denotes the electron coordinate. c) DFT calculations of binding modes at PbI_2-terminated interfaces with NC-PCBM (left) and NC-PCBA (right). d) DFT calculations of binding modes at CsI-terminated interfaces with NC-PCBM (left) and NC-PCBA (right). e) pDOS (left) and total DOS (right) at the PbI_2-terminated interfaces of NC-PCBA. f) pDOS (left) and total DOS (right) at the CsI-terminated interfaces of NC-PCBA. Overlays show the DOS for PCBA molecules compared to the first three layers of the $CsPbI_3$ slab.

various fields of optoelectronics. Paradoxically, HCs in most perovskite devices appear to be anomalously confined within the perovskite interior, defying expectations based on their temporal and spatial extension.[15–18] This critical bottleneck stems from the difficulty of HCs traversing the interfaces of heterogeneous systems, highlighting a fundamental challenge in translating the intrinsic properties of HCs in perovskites into practical applications. Previous impressive studies have provided valuable feasibility demonstrations for HC capture in specific heterogeneous systems combining perovskites with specific materials such as 4,7-diphenyl-1,10-phenanthroline and surface-cleaned graphene.[13,19,20] While these pioneering works have laid a crucial foundation, these isolated successes have also revealed the complexity of HC capture dynamics at perovskite interfaces. Beyond the inherent properties of the light-harvesting materials, numerous factors—such as the HC extraction capability of the extraction material, energy level alignment, the interfacial coupling between the two materials, etc.—may also impose constraints.[16,21–24] However, to date, a comprehensive understanding applicable to more generalized perovskite heterogeneous systems remains largely elusive. To bridge this gap and advance perovskite-based HC applications, it is imperative to identify the pivotal factors limiting the HC capture process and to devise effective strategies for surmounting these barriers. Considering the generous temporal window afforded by HCs in perovskites, particularly in their NC forms, we propose that electronic coupling at the heterogeneous interface may constitute a key determinant of HC capture deserving of intensified

focus. This electronic coupling fundamentally governs the probability of HCs surmounting interfacial energy transfer barriers (Figure 1b) in accordance with charge transfer theory.[25,26] While the significance of this factor has been corroborated in HC capture studies of other materials,[23,24] its role within perovskites remains to be fully elucidated.

Here, we exploit the nanoscale dimensions and accessible surfaces of perovskite NCs, alongside the chemical diversity of fullerenes to uncover this interplay. Through density functional theory (DFT) calculations, we show that effective interfacial bonding at the NC-fullerene junction induces synergistic electronic states, potentially establishing pathways for HC capture. Guided by these insights, we use the functional design of fullerenes to strategically engineer several contrasting $CsPbI_3$ NC (14.6 ± 1.5 nm, Figure S1, Supporting Information) -fullerene hybrid systems, achieving fine-tuning of their coupling to investigate HC capture dynamics. Our design strategy leads to the formation of ground-state complexes in certain of these systems, exhibiting effective coupling across a wide energy range, which we term state-coupled complexes. We validate the formation and characteristics of these complexes through distinctive interaction modes observed via fluorescence quenching spectroscopy and derivative absorption spectroscopy. Using transient absorption (TA) spectroscopy, we further investigate HC capture dynamics in these systems and discover that the formation of state-coupled complexes not only overcomes the initially forbidden HC capture within these hybrids but dramatically enhances it, achieving a ≈76% HC capture efficiency. These findings offer general insights that will allow for further understanding and manipulation of HC capture dynamics.

2. Results and Discussion

We initiated our study by exploring the impact of converting the methyl ester group of the widely used acceptor [6,6]-phenyl-C61-butyric acid methyl ester (PCBM) to a carboxylic acid group, yielding the acid-hydrolyzed derivative [6,6]-phenyl-C61-butyric acid (PCBA). Our DFT calculations reveal that this subtle modification profoundly alters the interfacial binding modes and electronic structure at the fullerene-$CsPbI_3$ perovskite junctions. After examining various relaxed configurations for both PCBA and PCBM on $CsPbI_3$ slabs (Figures S2 and S3, and Supplementary Note S1, Supporting Information), we identified the most energetically favorable and experimentally relevant interfacial configurations as shown in Figure 1c,d. In these configurations, PCBA predominantly interacts in its deprotonated carboxylate form, establishing chemical bonding with the $CsPbI_3$ surface. This modification replaces PCBM's physical adsorption with stronger chemical bonding for PCBA, irrespective of surface termination. The transition is accompanied by a dramatic increase in binding affinity, from ≤0.03 eV for PCBM to 4.1–4.2 eV for PCBA (Figure S3, Supporting Information), and significant interfacial charge redistribution (Figure S4, Supporting Information), which likely reduces charge transfer resistance.[27]

Further analysis of bond lengths and bond order (Table S1 and Supplementary Note S1, Supporting Information) confirms PCBA's chemical anchoring on the $CsPbI_3$ surface, characterized by bidentate chelating (two oxygen atoms from PCBA connecting to Pb) and bridging (two oxygen atoms bonding separately with Pb and Cs) modes. This configuration not only enhances stability compared to monodentate binding[28] but also induces resonant partial density of state (pDOS) structures among surface-bonded atoms (Figure 1e,f, left panels). Consequently, significant overlaps are observed in the DOS of PCBA and the first three layers of the $CsPbI_3$ slab across a broad energy range (Figure 1e,f, right panels), suggesting strong electronic coupling and possible wavefunction hybridization between the two materials.[29–31] We propose that these newly formed interfacial electronic structures could serve as efficient channels, potentially enhancing interfacial HC capture.[32,33]

Guided by the DFT insights, we engineered four distinct hybrid systems by combining $CsPbI_3$ NCs with PCBM, Bis(1-[3-(methoxycarbonyl) propyl]-1-phenyl)-[6.6]C62 ([Bis]PCBM), and their acid-hydrolyzed derivatives PCBA and [Bis]PCBA (See Experimental Section and Figures S5–S8, Supporting Information) to fine-tune the interfacial electronic coupling in these hybrids. To probe the critical interfacial interactions in these systems, we employed fluorescence quenching spectroscopy (**Figure 2a–c**; derived from Figure S9, Supporting Information), leveraging its sensitivity to weak and complex molecular interactions.[34,35] Our initial analysis focused on the $CsPbI_3$ NC-PCBM and NC-[Bis]PCBM systems. The fluorescence quenching data revealed a dynamic quenching mechanism, characterized by downward-curving Stern–Volmer plots (F_0/F versus Q), where F_0 represents the fluorescence intensity in the absence of fullerene, F is the fluorescence intensity in the presence of fullerene, and Q is the fullerene concentration (Figure 2b). This behavior can be quantified by the equation $F_0/\Delta F = f_a^{-1}K_a^{-1}[Q]^{-1}+f_a^{-1}$. Here, f_a represents the fraction of NCs with high surface accessibility to fullerene molecules, ΔF represents F_0-F, and K_a is the quenching constant of accessible NCs.[36] As illustrated in Figure 2a (upper panel), this interaction mode is characterized by transient, collision-based carrier transfer between NCs and fullerenes, occurring only under photoexcitation. This purely physical interaction results in the system reverting to its initial state post-illumination. The transient nature of these interactions precludes stable electronic coupling and inherently limits carrier transfer due to reliance on slow molecular diffusion.[11] These limitations persist despite the higher accessibility and quenching constant of [Bis]PCBM (f_a≈92%, K_a≈1.46×10^8 M^{-1}) compared to PCBM (f_a≈49%, K_a≈5.71×10^7 M^{-1}), underscoring that mere contact between NCs and fullerenes is not sufficient to create favorable conditions for effective HC capture.

In stark contrast to $CsPbI_3$ NC-PCBM/[Bis]PCBM systems, we uncovered a fundamentally distinct binding mechanism in $CsPbI_3$ NC-PCBA and NC-[Bis]PCBA hybrids, predominantly characterized by the formation of stable chemical complexes, with a minor contribution from collision-based interactions. This dual-nature binding, evidenced by distinctive two-stage Stern–Volmer plots (Figure 2c), manifests as an initial upward-curving feature followed by a linear relationship. The upward-curving feature signifies a cooperative effect where PCBA molecules partially form stable complexes with perovskites via chemical bonding (static quenching) and partially interact with perovskites through transient collisions (dynamic quenching).[37] Figure 2a (lower panel) visualizes the evolution of interactions in colloidal dispersion, revealing dynamic quenching modes, akin to those in $CsPbI_3$ NC-PCBM/[Bis]PCBM systems, while more significantly

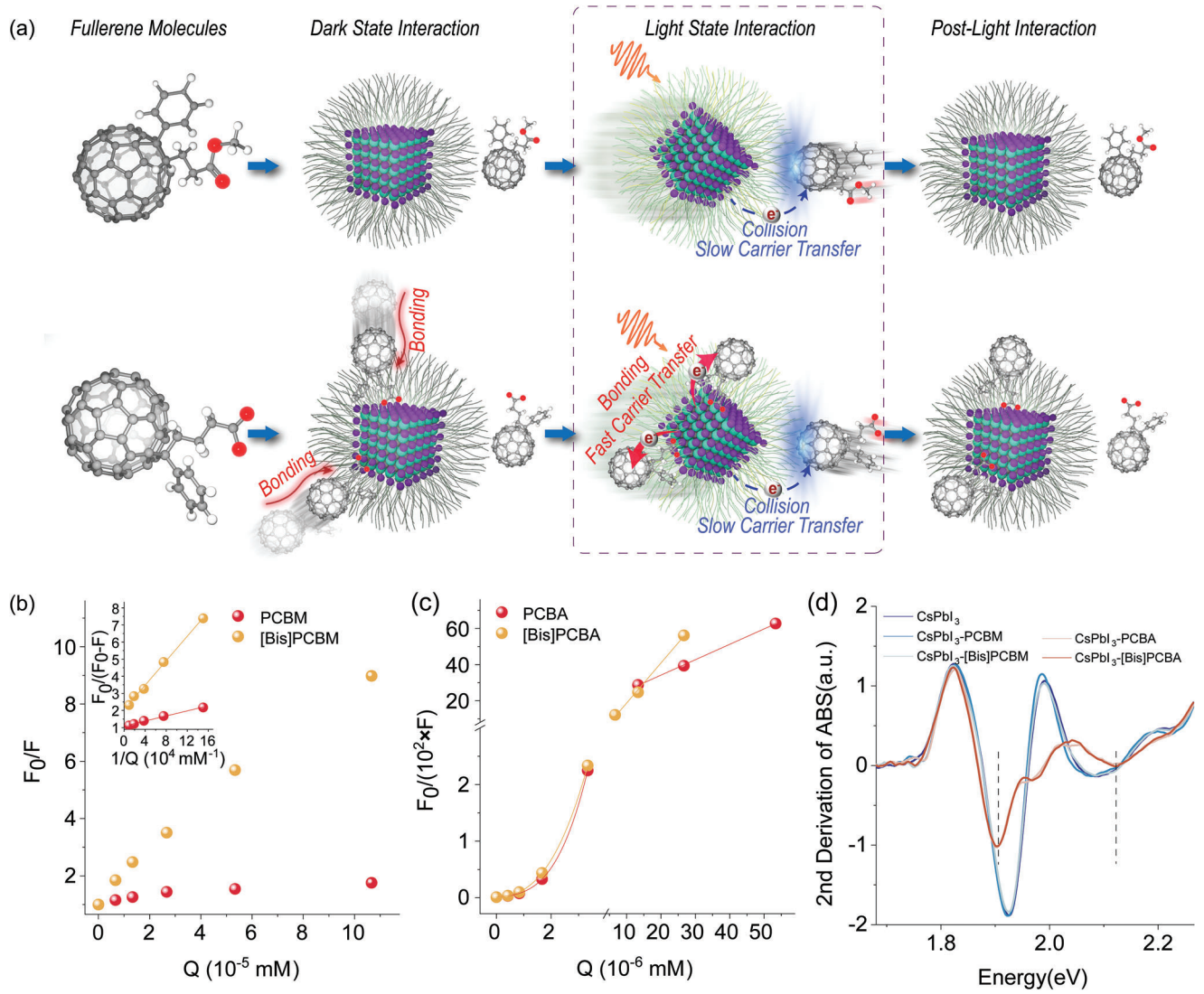

Figure 2. a) Schematic representation of the interactions between fullerene molecules and $CsPbI_3$ NCs. b) Stern–Volmer plots depicting the quenching of $CsPbI_3$ NC fluorescence by PCBM and [Bis]PCBM; the inset shows the modified Stern–Volmer plot. c) Stern–Volmer plots for PCBA and [Bis]PCBA quenching of $CsPbI_3$ NCs. d) Second derivative absorption spectra comparing $CsPbI_3$ NCs to $CsPbI_3$ NC-fullerene hybrid dispersions.

highlighting a distinct, light-independent chemical binding to a stable complex. We quantitatively described this phenomenon using a combined model: $F_0/F = [K_d([Q]+1)][K_b[Q]^n+1]$, where K_d and K_b represent quenching constants from transient collisions and stable bond formation respectively, and n indicates binding sites per NC (see Supplementary Note S2, Supporting Information). Significantly, our analysis revealed K_b values six orders of magnitude larger than K_d (Table S2), attributed to the high bonding stability and close contact distance of the stable complexes, which circumvent diffusion limitations and result in nonlinear quenching enhancement.[36,38] This formation of the stable binding mode is also evidenced by the efficient exciton dissociation observed in colloidal solutions (Figures S10, Supporting Information) potentially under the influence of a built-in electric field within the complex.[39] Moreover, the derived $n\approx2$ indicates that typically two PCBA or [Bis]PCBA molecules chemically bond to each NC. This is corroborated by X-ray photoelectron spectroscopy and infrared spectroscopy analyses, which show preferential anchoring of their deprotonated carboxylate form to uncapped atoms rather than through ligand exchange (Supplementary Note S3 and Figures S11 and S12, Supporting Information). Notably, the second derivative absorption spectra (Figure 2d) reveal significant changes in the electronic states of $CsPbI_3$ NCs upon binding with PCBA/[Bis]PCBA, but not with PCBM/[Bis]PCBM. These changes, observed at both the band edge and high energy levels, are solely attributed to the effective coupling in the $CsPbI_3$ NC-fullerene hybrids, as the spectral contribution of fullerene has been removed. This observation provides strong evidence for the formation of a state-coupled complex specifically in the $CsPbI_3$ NC-PCBA/[Bis]PCBA systems. At higher concentrations, binding site saturation leads to a linear relationship ($F_0/F = K_{d2}Q + b$), where excess PCBA molecules interact dynamically with preformed complexes.[34] Here, K_{d2} represents the dynamic quenching constant, and b accounts for

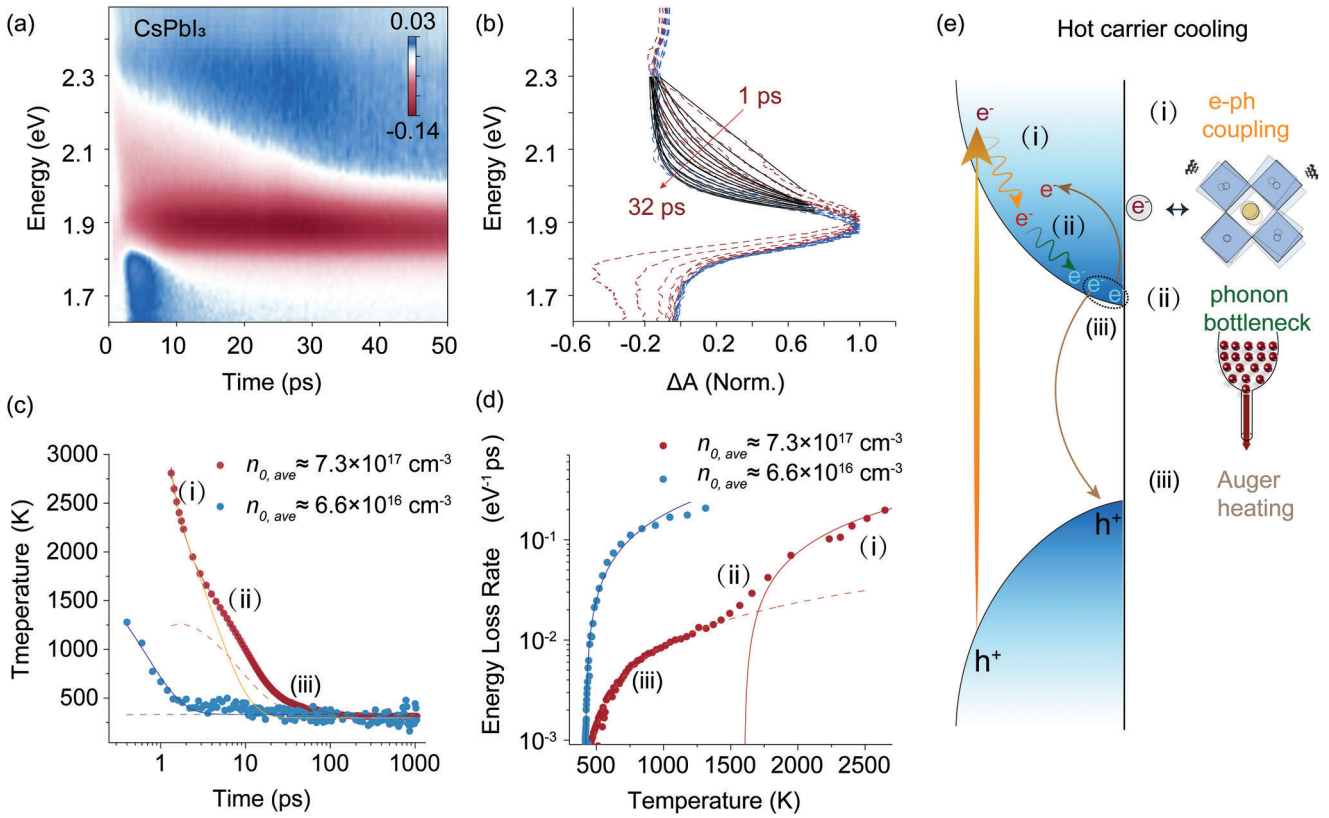

Figure 3. a) Pseudo color TA maps of intrinsic $CsPbI_3$ NCs excited by a 470 nm pump at $n_{0,ave}$≈7.3 × 10^{17} cm^{-3}. b) TA spectra higher energy tails fitted with the Fermi-Dirac distribution to determine HC temperature (T_c). The spectra were collected at time delays of 1, 1.7, 2.9, 4.1, 5.3, 6.5, 7.7, 8.9, 10.1, 11.3, 14, 17, 20, 23, 26, 29, and 32 ps after excitation. c) Time-dependent T_c profiles, with solid lines (red for $n_{0,ave}$≈7.3×10^{17} cm^{-3}, blue for $n_{0,ave}$≈6.6 × 10^{16} cm^{-3}) indicating TTM fits. Dashed lines show corresponding phonon temperatures. The solid orange line illustrates HC temperature decay under higher pump fluence, excluding Auger reheating effects. d) Energy loss rates as a function of HC temperature, with solid red and blue lines for LO-phonon emission model fits and dashed red line for Auger reheating model fits. e) Schematic of slow HC cooling mechanisms, highlighting electron–phonon coupling, phonon bottleneck, and Auger reheating effects.

the baseline shift caused by site saturation (refer to Supplementary Note S2, Supporting Information for additional explanation). The comparable magnitudes of K_{d2} and K_a for PCBM systems (Table S2, Supporting Information) support this transition to purely dynamic quenching. These findings demonstrate that our carboxylic acid functionalization profoundly alters NC-fullerene interactions, establishing stable chemical bonds crucial for electronic wavefunction coupling, thus overcoming limitations of purely transient interactions in PCBM/[Bis]PCBM systems and potentially facilitating more efficient HC capture.

To provide crucial insights into the effectiveness of various coupling regimes for HC capture, we quantitatively assessed HC dynamics across inherent NCs (**Figure 3**) and different NC-fullerene hybrids (**Figure 4**) using TA spectroscopy. In the TA spectra of $CsPbI_3$ NCs excited at 470 nm (Figure 3a), we observed a negative photobleaching peak (PB) at the band edge (≈1.88 eV) and high-energy tails (1.96–2.30 eV) reflecting the Fermi–Dirac distribution of HCs.[10] By fitting these high-energy tails (Figure 3b), we extracted carrier temperatures (T_c) from TA spectra after a 0.3–1 ps delay, ensuring HCs had reached quasi-equilibrium through carrier-carrier scattering.[40] The extracted T_c and energy loss rates ($J_e = -1.5k_b \cdot dT_c/dt$) revealed distinct HC cooling behaviors under different excitation intensities (Figure 3c,d). At low pump fluence (average carrier density $n_{0,ave}$ ≈ 6.6 × 10^{16} cm^{-3}, acquired from Figure S13, Supporting Information), HCs rapidly cooled to lattice temperature within 2 ps due to carrier-longitudinal optical (LO) phonon scattering,[41] with a fitted LO-phonon scattering time τ_{LO} of ≈0.51 ps (see blue scatter and blue fit line in Figure 3d and fitting methods in Supplementary Note S4, Supporting Information). As described in Figure 1a, providing an extended HC extraction window is crucial for efficient HC capture. To achieve this goal, we deliberately increased the excitation intensity, aiming to extend HC lifetimes. Notably, at higher fluence ($n_{0,ave}$ ≈ 7.3 × 10^{17} cm^{-3}), we observed significantly extended HC cooling times, with T_c taking ≈70 ps to reach room temperature (Figure 3c, red scatter). We attribute this prolonged cooling to the synergistic effects of hot phonon bottleneck and Auger reheating,[10,11] as illustrated in Figure 3e. This interpretation is supported by the slow decrease in phonon temperature (Figure 3c, red dashed line) obtained through three-temperature model (TTM) fitting,[42,43] and the comparison between actual and Auger-neglected HC temperature curves (Figure 3c, orange line). The contributions of different processes to J_e are detailed in Figure 3d, with the red solid fit line representing the electron-LO phonon emission model, the red dashed fit line showing Auger reheating, and their

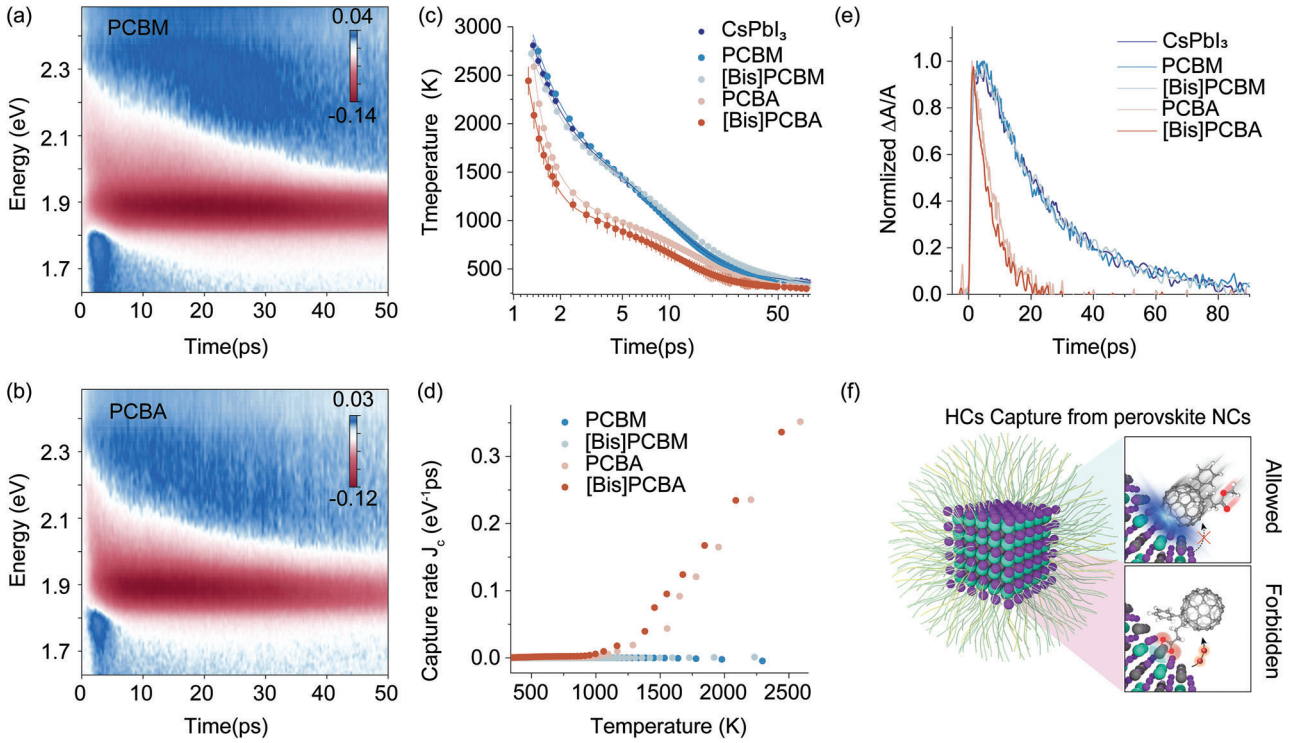

Figure 4. Pseudo color TA maps of a) $CsPbI_3$ NC-PCBM hybrids and b) $CsPbI_3$ NC-PCBA hybrids, excited by a 470 nm pump at $n_{0,\,ave}$≈7.3 × 10^{17} cm^{-3}. c) Time-dependent profiles of T_c for pristine NCs and various NC-fullerene hybrids. d) Energy capture rates are plotted as a function of HC temperature. e) IBP kinetics illustrate the average decay constant τ for HCs. f) Diagram illustrating the influence of coupling on HC capture.

intersection suggesting the hot phonon bottleneck effect (see theories and fitting models in Supplementary Notes S4 and S5, Supporting Information).

Building upon observations of extended HC lifetimes, we explored HC capture dynamics within various NC-fullerene hybrids, all subjected to uniform excitation conditions. To ensure consistent $n_{0,\,ave}$ across all samples, we maintained stable NC concentrations and leveraged the minimal absorption characteristics of fullerenes, as confirmed in Figures S8 and S14 (Supporting Information). Our analysis of TA spectra (see Figures 4a,b; Figures S15 and S16, Supporting Information) highlighted a significant contrast in HC dynamics: $CsPbI_3$ NC-PCBM/[Bis]PCBM hybrids exhibited negligible spectral changes relative to pristine NCs, whereas $CsPbI_3$ NC-PCBA/[Bis]PCBA hybrids demonstrated a pronounced acceleration in the decay of high-energy tails. This behavior, indicating a marked enhancement in HC capture, was further evidenced by a substantial reduction of T_c in PCBA/[Bis]PCBA systems—while T_c remained nearly identical in PCBM/[Bis]PCBM systems compared to pristine $CsPbI_3$, as detailed in Figure 4c.

To isolate the effects of interfacial transfer from intrinsic HC cooling, we analyzed the energy capture rates through carrier capture-induced electronic energy power loss rates, J_e (fullerene) = J_e (NCs) − J_e (hybrids), utilizing the data presented in Figure 4c. The response of J_e (PCBA/[Bis]PCBA) was notably temperature-dependent, exhibiting a significant increase, particularly past 850K, highlighting the preferential capture of HCs—a stark contrast to the negligible values observed in PCBM/[Bis]PCBM-based systems, as shown in Figure 4d. Furthermore, to quantify capture efficiency (η), we used the kinetic curve at the isosbestic point (IBP), located at ≈1.96 eV on the higher energy side of the ground state PB signal to provide a consistent reference for determining the averaged decay constant (τ) of the HCs (see Supplementary Movie S1, Supporting Information for a detailed dynamic visualization). Employing the equation $\eta = 1 - \tau_{hybrids}/\tau_{NCs}$, we calculated the capture efficiencies, revealing efficiencies up to 66% for PCBA and up to 76% for [Bis]PCBA (illustrated in Figure 4e, τ data is summarized in Table S3, Supporting Information). While extended HC lifetimes appreciably contribute to these efficiencies (see comparative results with $n_{0,\,ave}$≈6.6 × 10^{16} cm^{-3} in Figure S16, Supporting Information), our analysis confirms that interfacial coupling is the predominant factor influencing HC capture dynamics, as depicted in Figure 4f. This reversal from prohibited to efficient HC capture in our NC and fullerene hybrid systems underscores the transformative impact of our molecular design strategy. It highlights the indispensable role of tailored interfacial electronic coupling in advancing the performance of next-generation optoelectronic devices. We believe that the insights and strategies developed here have broad applicability and could be beneficial for other systems as well.

3. Conclusion

In summary, our study demonstrates that engineering donor–acceptor coupling is crucial for optimizing HC capture dynamics, offering a more effective approach than simply extending HC lifetimes. Our DFT calculations have shown that effective

interfacial bonding at the NC-fullerene junction induces synergistic electronic states, potentially establishing new pathways for HC capture. By strategically modifying fullerene structures, we engineered stable chemical bonds with perovskite NCs, controlling the formation of differently coupled perovskite NC-fullerene hybrid systems. TA spectroscopy further indicates that highly efficient HC capture in perovskite-fullerene hybrids occurs only when these materials form state-coupled complexes. The creation of HC capture channels within their binding sites post-coupling significantly contributes to this efficiency. Our research offers important insights into manipulating HC capture dynamics in perovskite heterojunction. The knowledge and strategy gained here are of universal meaning, taking an important step forward for HC photovoltaics.

4. Experimental Section

Materials: Oleic acid (OA, 90%), oleylamine (OAm, 70%), octadecene (ODE, technical grade 90%), cesium carbonate (Cs_2CO_3, 99.99%), PCBM (>99.5%), [Bis]PCBM (>99.5%), 4-(1′,5′-Dihydro-1′-methyl-2′H-[5,6]fullereno-C_{60}-Ih-[1,9-c]-pyrrol-2′-yl)benzoic acid (>99%), tetrahydrofuran (THF, ≥99.9%), chlorobenzene (CB, 99.8%), tetrahydrofuran-d_8 (≥99.5 atom% D), chlorobenzene-d_5 (≥99.5 atom% D), hydrochloric acid (HCl, 37 wt% in H_2O), methanol (MeOH, ≥99.9%), and acetic acid (HAc, ≥99%) were purchased from Sigma–Aldrich. Lead iodide (PbI_2, 99.99%), methyl acetate (MeOAc, anhydrous 99.5%), n-hexane (99%), and toluene (98%) were purchased from Wako.

Synthesis of Colloidal $CsPbI_3$ NCs: The synthesis followed a previously reported method with slight modifications.[44] Briefly, 2.1324 g OA, 0.6 g Cs_2CO_3, and 20 mL ODE were mixed in a 100 mL three-neck flask, degassed at 120 °C under vacuum for 40 min, and then maintained at 120 °C under N_2 until needed. Separately, 0.4 g PbI_2 and 20 mL ODE were mixed in a 50 mL three-neck flask, degassed at 120 °C under vacuum for 30 min, and kept at 120 °C under N_2. Preheated OA and OAm (3 mL each at 60 °C) were injected into the PbI_2 solution and maintained at 120 °C for 30 min. The mixture was then heated to 160 °C under N_2, and 3.2 mL of the Cs-oleate precursor was immediately injected. After reacting for 5–8 s, the reaction was quenched using an ice bath. The colloidal solution was divided into four tubes, and 45 mL MeOAc was added to each, followed by centrifugation at 8500 rpm for 4 min. The precipitated NCs were dispersed in 4 mL n-hexane, stored at 4 °C for 24 h, and then centrifuged at 4000 rpm for 2 min. Before use, the NC solution was centrifuged at 7000 rpm for 5 min, the supernatant was dried under N_2, and the residue was dispersed in n-hexane to obtain a 50 mg mL^{-1} $CsPbI_3$ NC solution.

Synthesis of PCBA and [Bis]PCBA: PCBA was obtained by hydrolyzing PCBM.[45] A solution of PCBM (100 mg, 0.147 mmol) in CB (20 mL) was refluxed under N_2 for 3 h. HCl (12 mmol mL^{-1} , 6 mL) and HAc (30 mL) were added in one portion, and the mixture was refluxed for 16 h. The solvent was removed under reduced pressure, and the residue was purified by precipitation from MeOH three times to obtain PCBA as a brown solid. [Bis]PCBA was synthesized similarly, adjusting molar ratios accordingly. PCBM and [Bis]PCBM were dissolved in CB (0.02 mmol mL^{-1}); PCBA and [Bis]PCBA were dissolved in a 1:1 (v/v) mixture of CB and THF (0.02 mmol mL^{-1}). The solutions were stirred at 50 °C for 30 min.

Preparation of CsPbI3 NC-Fullerene Hybrids: $CsPbI_3$ NC solution (50 µL, in n-hexane) was added to 2 µL of fullerene derivative solutions and stirred for 2 min. The colors of NC solutions mixed with PCBM and [Bis]PCBM remained nearly unchanged, while those mixed with PCBA and [Bis]PCBA quickly turned black and precipitated upon centrifugation at 4000 rpm for 2 min. The precipitates were redispersed in toluene and centrifuged again at 4000 rpm for 2 min. The NCs were dried under N_2 and redispersed in 500 µL CB or toluene, followed by ultrasonication for 30 min. The influence of THF was negligible in theese experiments.

Characterization: Phase identification was performed using powder X-ray diffraction (TTR-III, Rigaku). Morphology and crystal structure were characterized using transmission electron microscopy (JEM-2100F). UV–vis absorption spectra were measured using a spectrophotometer (HITACHI, U-3900H). Attenuated total reflection Fourier transform infrared (FTIR) spectra were recorded using a Nicolet 6700 spectrophotometer. X-ray photoelectron spectroscopy data were collected on a JPS-90MX (JEOL). Nuclear magnetic resonance spectra were recorded with a JEOL ECA-500 (500 MHz) instrument. Excitation intensity-dependent photoluminescence (PL), transient PL, and PL for Stern–Volmer plots were recorded using a PL system from TOKYO INSTRUMENT, INC. A 473 nm pulsed diode laser (pulse width 90 ps, repetition up to 100 MHz, peak power 4 mW) served as the excitation source. An adjustable neutral density filter controlled the excitation intensity. PL detection was performed using a photomultiplier tube with a time-correlated single-photon counting module. TA measurements were performed using a femtosecond TA setup. The laser source was a titanium laser (CPA-2010, Clark-MXR Inc.) at 775 nm wavelength, 1 kHz repetition rate, and 120 fs pulse width. The light was split into two parts: one generated white light for the probe beam via a sapphire plate, and the other pumped an optical parametric amplifier (OPA, TOAPS, Quantronix) to produce tunable light from 290 nm to 3 µm. A 470 nm pump light was used to excite the NCs. The pseudo-color TA maps were plotted using Python 3.8.10, employing the Matplotlib library for visualization.

DFT Calculations: DFT calculations were implemented in the Vienna Ab initio Simulation Package.[46] The Perdew–Burke–Ernzerhof functional within the Generalized Gradient Approximation was employed. The outermost s, p, and d (in the case of Pb) electrons were treated as valence electrons, with their interactions with the remaining ions modeled by pseudopotentials generated within the Projector-Augmented Wave method.[47,48] An energy cutoff of 500 eV and a k-point scheme of 4 × 4 × 1 were utilized to achieve energy and force convergence of 0.1 meV and 20 meV $Å^{-1}$, respectively. For the PDOS calculation, the Brillouin zone was sampled using an 8 × 8 × 1 k-mesh. A $CsPbI_3$ surface models were constructed with the top and bottom surfaces being the [0 0 1] facets terminated by CsI and PbI_2 layers, respectively (Figure S2, Supporting Information). The surfaces were modeled using slab models consisting of (2 × 2) cells in the x and y directions and five repeating units (20 Cs atoms, 20 Pb atoms, and 60 I atoms). To investigate the effect of NC surface ligands, the slab model was passivated by oleate ($C_{18}H_{33}O_2^-$:OA^-), PCBA (both its carboxylate (PCBA-COO^-) and carboxylic acid (PCBA-COOH) forms), or PCBM on CsI-termination and PbI_2-termination, respectively, with different configurations (see atomistic molecular models of ligands in Figure S3, Supporting Information). A vacuum of 20 Å in the z-direction was set to avoid periodic effects, and dipole correction along the z-direction was considered. The ligand slab model for investigating the surface of NCs has been validated in the previous works.[49,50] During these structural optimizations, ions on the bottom were fixed to mimic the bulk nature, while all other ions (including the ligands on top of the surface) were allowed to relax and optimize to their minimum energy configuration. Specifically for the negatively charged ligands PCBA-COO^- and OA^-, iodide ions (I^-) on the $CsPbI_3$ surface were replaced to maintain charge neutrality and prevent the formation of unstable radicals during calculations. The ligand binding affinity (E_b) of the ligands in Figure S3 (Supporting Information) to the NC surface was computed as: $E_b = (E_{tot} - E_{NCs} - E_{lig})/S$, where E_{tot} is the energy of the slab model passivated with ligands, E_{NCs} is the energy of the slab model (the perovskite NCs) without the ligand, E_{lig} is the energy of the ligand, and S is the numbers of the ligands in the slab model. Bond order calculations were carried out using DDEC6 charge partitioning, as implemented in the Chargemol code.[51]

Supporting Information

Supporting Information is available from the Wiley Online Library or from the author.

Acknowledgements

Y.L., J.J., and D.W. contributed equally to this work. The authors are very grateful to Prof. James Lloyd-Hughes (Department of Physics, University of Warwick, United Kingdom), and Dr. Maurizio Monti (Institute for Physics and Astronomy, Denmark) for their kind providing of the TTM fitting code and patient explanations about their code. The authors also appreciate the meaningful help on FTIR analysis from Prof. Ishida Takayuki (The University of Electro-Communications, Japan). This work was supported by the Japan Science and Technology Agency (JST) Mirai program (JPMJMI17EA), MEXT KAKENHI Grant (26286013, 17H02736), JST SPRING (Grant Number JPMJSP2131). S.T. and J.J. acknowledge funding by the Computational Sciences for Energy Research (CSER) tenure track program of Shell and NWO (Project number 15CST04-2) and NWO START-UP, the Netherlands.

Conflict of Interest

The authors declare no conflict of interest.

Data Availability Statement

The data that support the findings of this study are available from the corresponding author upon reasonable request.

Keywords

coupling, fullerene, hot carrier capture, interfacial bonding, perovskite

Received: August 26, 2024
Revised: October 25, 2024
Published online:

[1] C. A. Nelson, N. R. Monahan, X. Y. Zhu, *Energy Environ. Sci.* **2013**, *6*, 3508.
[2] M. A. Green, *Third generation photovoltaics*, Springer, Berlin, Germany **2006**.
[3] K. K. Paul, J. H. Kim, Y. H. Lee, *Nat. Rev. Phys.* **2021**, *3*, 178.
[4] A. J. Nozik, *Nat. Energy* **2018**, *3*, 170.
[5] N. M. Gabor, J. C. W. Song, Q. Ma, N. L. Nair, T. Taychatanapat, K. Watanabe, T. Taniguchi, L. S. Levitov, P. Jarillo-Herrero, *Science* **2011**, *334*, 648.
[6] W. Shockley, H. J. Queisser, *J. Appl. Phys.* **1961**, *32*, 510.
[7] L. Zhou, D. F. Swearer, C. Zhang, H. Robatjazi, H. Zhao, L. Henderson, L. Dong, P. Christopher, E. A. Carter, P. Nordlander, N. J. Halas, *Science* **2018**, *362*, 69.
[8] Y. Dong, J. Choi, H. K. Jeong, D. H. Son, *J. Am. Chem. Soc.* **2015**, *137*, 5549.
[9] H. Zhu, K. Miyata, Y. Fu, J. Wang, P. P. Joshi, D. Niesner, K. W. Williams, S. Jin, X. Y. Zhu, *Science* **2016**, *353*, 1409.
[10] Y. Yang, D. P. Ostrowski, R. M. France, K. Zhu, J. van de Lagemaat, J. M. Luther, M. C. Beard, *Nat. Photonics* **2016**, *10*, 53.
[11] J. Fu, Q. Xu, G. Han, B. Wu, C. H. A. Huan, M. L. Leek, T. C. Sum, *Nat. Commun.* **2017**, *8*, 845.
[12] L. Dai, Z. Deng, F. Auras, H. Goodwin, Z. Zhang, J. C. Walmsley, P. D. Bristowe, F. Deschler, N. C. Greenham, *Nat. Photonics* **2021**, *15*, 696.
[13] M. Li, S. Bhaumik, T. W. Goh, M. S. Kumar, N. Yantara, M. Grätzel, S. Mhaisalkar, N. Mathews, T. C. Sum, *Nat. Commun.* **2017**, *8*, 14350.
[14] Z. Guo, Y. Wan, M. Yang, J. Snaider, K. Zhu, L. Huang, *Science* **2017**, *356*, 59.
[15] J. J. Shi, Y. M. Li, Y. S. Li, D. M. Li, Y. H. Luo, H. J. Wu, Q. B. Meng, *Joule* **2018**, *2*, 879.
[16] M. Li, J. Fu, Q. Xu, T. C. Sum, *Adv. Mater.* **2019**, *31*, 1802486.
[17] M. A. Green, A. Ho-Baillie, H. J. Snaith, *Nat. Photonics* **2014**, *8*, 506.
[18] W. E. Sha, H. Zhang, Z. S. Wang, H. L. Zhu, X. Ren, F. Lin, A. K. Y. Jen, W. C. Choy, *Adv. Energy Mater.* **2018**, *8*, 1701586.
[19] S. S. Lim, D. Giovanni, Q. Zhang, A. Solanki, N. F. Jamaludin, J. W. M. Lim, N. Mathews, S. Mhaisalkar, M. S. Pshenichnikov, T. C. Sum, *Sci. Adv.* **2019**, *5*, eaax3620.
[20] H. Hong, J. Zhang, J. Zhang, R. Qiao, F. Yao, Y. Cheng, C. Wu, L. Lin, K. Jia, Y. Zhao, Q. Zhao, P. Gao, J. Xiong, K. Shi, D. Yu, Z. Liu, S. Meng, H. Peng, K. Liu, *J. Am. Chem. Soc.* **2018**, *140*, 14952.
[21] D. König, K. Casalenuovo, Y. Takeda, G. Conibeer, J. F. Guillemoles, R. Patterson, L. M. Huang, M. A. Green, *Phys. E. Low-Dimens. Syst. Nanostructures* **2010**, *42*, 2862.
[22] R. T. Ross, A. J. Nozik, *J. Appl. Phys.* **1982**, *53*, 3813.
[23] W. A. Tisdale, K. J. Williams, B. A. Timp, D. J. Norris, E. S. Aydil, X. Y. Zhu, *Science* **2010**, *328*, 1543.
[24] R. Austin, Y. R. Farah, T. Sayer, B. M. Luther, A. Montoya-Castillo, A. T. Krummel, J. B. Sambur, *Proc. Natl. Acad. Sci. U.S.A.* **2023**, *120*, 2220333120.
[25] R. A. Marcus, N. Sutin, *Biochim. Biophys. Acta, Rev. Bioenerg.* **1985**, *811*, 265.
[26] D. L. Dexter, *J. Chem. Phys.* **1953**, *21*, 836.
[27] T. Li, J. Xu, R. Lin, S. Teale, H. Li, Z. Liu, C. Duan, Q. Zhao, K. Xiao, P. Wu, B. Chen, S. Jiang, S. Xiong, H. Luo, S. Wan, L. Li, Q. Bao, Y. Tian, X. Gao, J. Xie, E. H. Sargent, H. Tan, *Nat. Energy* **2023**, *8*, 610.
[28] A. E. Martell, R. D. Hancock, *Metal complexes in aqueous solutions*, Springer Science & Business Media, Berlin, Germany **2013**.
[29] Q. Wei, H. Ren, J. Liu, Q. Liu, C. Wang, T. W. Lau, L. Zhou, T. Bian, Y. Zhou, P. Wang, Q. Lei, O. F. Mohammed, M. Li, J. Yin, *ACS Energy Lett.* **2023**, *8*, 4315.
[30] J. Yin, D. Cortecchia, A. Krishna, S. Chen, N. Mathews, A. C. Grimsdale, C. Soci, *J. Phys. Chem. Lett.* **2015**, *6*, 1396.
[31] G. Grancini, M. Maiuri, D. Fazzi, A. Petrozza, H. J. Egelhaaf, D. Brida, G. Cerullo, G. Lanzani, *Nat. Mater.* **2013**, *12*, 29.
[32] T. Virgili, A. Calzolari, I. Suárez López, B. Vercelli, G. Zotti, A. Catellani, A. Ruini, F. Tassone, *J. Phys. Chem. C* **2013**, *117*, 5969.
[33] B. W. Caplins, D. E. Suich, A. J. Shearer, C. B. Harris, *J. Phys. Chem. Lett.* **2014**, *5*, 1679.
[34] C. Albrecht, *Anal. Bioanal. Chem.* **2008**, *390*, 1223.
[35] P. Lehner, C. Staudinger, S. M. Borisov, I. Klimant, *Nat. Commun.* **2014**, *5*, 4460.
[36] S. Lehrer, *Biochemistry* **1971**, *10*, 3254.
[37] H. Chen, S. S. Ahsan, M. E. B. Santiago-Berrios, H. D. Abruña, W. W. Webb, *J. Am. Chem. Soc.* **2010**, *132*, 7244.
[38] J. R. Albani, in *Structure and Dynamics of Macromolecules: Absorption and Fluorescence Studies*, (Ed: J. R. Albani), Elsevier Science, Amsterdam **2004**.
[39] J. Shi, Y. Li, J. Wu, H. Wu, Y. Luo, D. Li, J. J. Jasieniak, Q. Meng, *Adv. Optical Mater.* **2020**, *8*, 1902026.
[40] Q. Wei, J. Yin, O. M. Bakr, Z. Wang, C. Wang, O. F. Mohammed, M. Li, G. Xing, *Angew. Chem., Int. Ed.* **2021**, *60*, 10957.
[41] J. Chen, M. E. Messing, K. Zheng, T. Pullerits, *J. Am. Chem. Soc.* **2019**, *141*, 3532.
[42] J. C. Johannsen, S. Ulstrup, F. Cilento, A. Crepaldi, M. Zacchigna, C. Cacho, I. C. E. Turcu, E. Springate, F. Fromm, C. Raidel, T. Seyller, F. Parmigiani, M. Grioni, P. Hofmann, *Phys. Rev. Lett.* **2013**, *111*, 027403.
[43] M. Monti, K. D. G. I. Jayawardena, E. Butler-Caddle, R. M. I. Bandara, J. M. Woolley, M. Staniforth, S. R. P. Silva, J. Lloyd-Hughes, *Phys. Rev. B* **2020**, *102*, 245204.
[44] A. Swarnkar, A. R. Marshall, E. M. Sanehira, B. D. Chernomordik, D. T. Moore, J. A. Christians, T. Chakrabarti, J. M. Luther, *Science* **2016**, *354*, 92.

[45] Q. Wei, T. Nishizawa, K. Tajima, K. Hashimoto, *Adv. Mater.* **2008**, *20*, 2211.
[46] G. Kresse, J. Furthmüller, *Comput. Mater. Sci.* **1996**, *6*, 15.
[47] G. Kresse, D. Joubert, *Phys. Rev. B* **1999**, *59*, 1758.
[48] P. E. Blöchl, *Phys. Rev. B* **1994**, *50*, 17953.
[49] J. Jiang, F. Liu, Q. Shen, S. Tao, *J. Mater. Chem. A* **2021**, *9*, 12087.
[50] F. Liu, J. Jiang, T. Toyoda, M. A. Kamarudin, S. Hayase, R. Wang, S. Tao, Q. Shen, *ACS Appl. Nano Mater.* **2021**, *4*, 3958.
[51] T. A. Manz, N. G. Limas, *RSC Adv.* **2016**, *6*, 47771.